Universiteit Antwerpen

This item is the archived peer-reviewed author-version of:

Atomic-scale investigation of the heterogeneous precipitation in the E ($Al_{18}Mg_3Cr_2$) dispersoid of 7075 aluminum alloy

Reference:
Ding Lipeng, Zhao Lv, Weng Yaoyao, Schryvers Dominique, Liu Qing, Idrissi Hosni.- Atomic-scale investigation of the heterogeneous precipitation in the E ($Al_{18}Mg_3Cr_2$) dispersoid of 7075 aluminum alloy
Journal of alloys and compounds - ISSN 0925-8388 - 851(2021), 156890
Full text (Publisher's DOI): https://doi.org/10.1016/J.JALLCOM.2020.156890
To cite this reference: https://hdl.handle.net/10067/1735030151162165141

uantwerpen.be
Institutional repository IRUA

Atomic-scale investigation of the heterogeneous precipitation in the E ($Al_{18}Mg_3Cr_2$) dispersoid of 7075 aluminum alloy

Lipeng Ding[a,b,c*], Lv Zhao[d], Yaoyao Weng[e], Dominique Schryvers[c], Qing Liu[a], Hosni Idrissi[b,c]

[a] Key laboratory for Light-weight Materials, Nanjing Tech University, Nanjing 211816, PR China

[b] UCLouvain, Institute of Mechanics, Materials and Civil Engineering, IMAP, 1348 Louvain-la-Neuve, Belgium

[c] Electron Microscopy for Materials Science (EMAT), Department of Physics, University of Antwerp, Groenenborgerlaan 171, B-2020, Belgium

[d] Department of Mechanics, Huazhong University of Science and Technology, Wuhan, PR China

[e] School of Materials Science and Engineering, Nanjing Institute of Technology, Nanjing 211167, PR China

*Corresponding author.

E-mail address: lipeng.ding@njtech.edu.cn

Abstract

The heterogeneous precipitation of the η ($MgZn_2$) phase on the E ($Al_{18}Mg_3Cr_2$) dispersoids of the 7075 aluminum alloy was systematically investigated by atomic resolution high-angle annular dark-field scanning transmission electron microscopy (HAADF-STEM) and energy dispersive X-ray spectrometry (EDX). It is found that coarse η particles are heterogeneously precipitated at the E particle interface after water quenching and isothermal aging at 120ºC. The incoherent E/Al interface is responsible for the high tendency of heterogeneous precipitation of the η phase. Two different orientation relationships (ORs) between the η, E and Al matrix are identified: OR1 $[2\bar{1}\bar{1}0]_\eta$// $[011]_E$ // $[\bar{1}12]_{Al}$, $(01\bar{1}0)_\eta$ // $(13\bar{3})_E$ // $(201)_{Al}$, OR2 $[\bar{1}12]_E$ // $[0001]_\eta$// $[011]_{Al}$, $(01\bar{1}0)_\eta$ // $(220)_E$ // $(34\bar{4})_{Al}$. The η phase is preferential to nucleate along the $\{111\}_E$ or the $\{220\}_E$ planes, depending on its OR. The heterogeneous nucleation of η phase on the E particle could stabilize the E/Al interface by introducing a coherent E/η interface, which increases the drive force of heterogeneous precipitation. The reorientation of η phase and mutual diffusion of solute atoms could assist the coherency of the E/η interface. The present results suggest that increasing the coherency of the E/Al interface is a promising method to suppress the heterogeneous precipitation of the η phase.

Key words: Aluminum alloys; heterogeneous precipitation; dispersoid; HAADF-STEM

1. Introduction

The ultra-high strength 7075 (Al-Zn-Mg-Cu) alloy has been widely used in aeronautic and astronautic fields due to its excellent mechanical properties, such as high specific strength and good corrosion resistance [1, 2]. The strengthening of the alloy is achieved mainly by the dispersive precipitation of high-density nano-sized precipitates through aging treatment [3]. The precipitation sequence of Al-Zn-Mg-Cu alloys has been suggested as: SSSS → GP zones → η′ → η [4]. Among various precipitates, the η′ phase is generally believed to be responsible for the maximum strength at peak aging [5]. The η phase is an equilibrium hexagonal $MgZn_2$ Laves phase, which exhibits 11 reported orientation relationships (ORs) with the Al matrix, namely η_1 to η_{11} [6]. However, this alloy suffers from high quench sensitivity, which causes a loss of age-hardening response during slow quench cooling. In general, the quench sensitivity of the Al-Zn-Mg-Cu alloys is primarily associated with dispersoid particles and (sub)grain boundaries, which promote heterogeneous precipitation of the η phase. This leads to depletion of solute atoms in solid solution and hence lowers achievable strength and hardness [7-9]. The dispersoids, usually containing transition elements such as Mn, Cr and V, are formed during homogenization process. On the one hand, the dispersoids could suppress the recrystallization, grain growth and improve the fracture toughness of the alloys, on the other hand, the dispersoids can act as nucleation sites for coarse, non-hardening η phase, and hence increase the quench sensitivity [10, 11].

The $Al_{18}Mg_3Cr_2$, referred to as E phase, is a typical Cr-containing dispersoid formed in the 7075 alloy during homogenization [12]. The E dispersoid can effectively inhibit recrystallization, control grain growth, promote a more uniform deformation and reduce grain boundary stress concentration, and, as a consequence, delay the crack initiation [13]. However, pronounced heterogeneous precipitation of the η phase occurs at the interface of the E phase during quenching from high temperature, which consumes the solute atoms and vacancies, and thus leads to a considerable reduction in strength [14]. The suitability of dispersoids as nucleation sites depends on their interface structure with the Al matrix, which is determined by their composition, crystal structure and OR with the Al matrix. Therefore, proper characterization of the structure and chemistry of the E phase is essential to control the quench sensitivity of the alloy. Samson et al. [15] identified the structure of the E phase by X-ray diffraction (XRD) as an fcc structure with lattice parameter a=1.4526nm and space group Fd-3m. Ayer et al. [16] studied the crystal structure and composition of the E phase by XRD and convergent beam electron diffraction (CBED). They proposed that the composition of the E phase varies slightly with the aging treatment, up to 7 at.% Cu, Zn and Ti are substituted within the E phase. Moreover, some disordered regions are found within the E phase, and the degree of disorder varied from particle to particle. Due to the negative effect of heterogeneous

precipitation on the E particle, the Cr is gradually replaced by Zr in the new designed 7055 alloy, however, the Cr-containing 7075 alloy is still under large scale application due to its low cost. Therefore, suppress the heterogeneous precipitation of the η phase is of significantly importance for the property improvement of this alloy.

Although several works [14, 17] have investigated the negative effect of the E dispersoid on the quench sensitivity of the Al-Zn-Mg-Cu alloy, little work has been devoted to the understanding of the underlying mechanism of heterogeneous precipitation on the E phase, which requires an atomic scale characterization of the interface structure between the E phase and the Al matrix. Till now, the interface structure, composition and OR between the E, η and Al matrix still remain elusive, which limits the development of new alloys presenting low quench sensitivity. In the present work, the heterogeneous precipitation behaviour of the η phase on the E dispersoid is systematically studied by atomic-resolution high angle annular dark-field scanning transmission electron microscopy (HAADF-STEM) and STEM X-ray mapping.

2. Materials and Methods

A commercial 7075 aluminum alloy with composition Al-5.85Zn-2.51Mg-1.65Cu-0.19Cr-0.1Fe-0.04Zr-0.03Mn-0.05Ti (wt.%) was used in the present investigation. After solution treatment at 470^{o}C for 1h and water quenching to room temperature, the alloy was first aged at 120^{o}C for 24h to produce the peak-aged stage, and then the peak-aged sample was further aged at 170^{o}C for 6h to obtain a slightly over-aged condition. The HAADF-STEM characterization was performed using a FEI Titan 80-300 “cube” microscope with aberration correctors, which achieves a ~ 0.1nm probe size with a beam current of ~ 50pA and a convergence semi-angle of ~ 21mrad. The 3 mm bulk TEM samples were thinned by electropolishing using a Struers TenuPol-3 machine and an electrolyte of 30% HNO_3 in methanol. The electropolishing was conducted at a temperature in a range of -25^{o}C to -30^{o}C yielding a current of 50mA at a set voltage of 15V.

3. Results

3.1 Structure characteristic of the E phase

Fig. 1(a) shows a low-magnification HAADF-STEM image of a typical region in the over-aged 7075 alloy viewed along the <110> zone axis. It can be seen that a uniform distribution of nano-sized particles with different sizes is formed in the alloy. The first type is the η′/η phase with a size ranging from 2-10 nm, which are the main strengthening precipitates formed in this alloy (as indicated by the white arrows in Fig. 1). The second type is the E phase, which exhibits a lath or tetragonal-shaped morphology with a size ranging from 100 nm to 200 nm.

Heterogeneous precipitation of the η phase at the E/Al interface is supposed to occur as evidenced by the brighter layers formed at the border of the E particles (as marked by the black arrows in Fig. 1). It can be deduced that the tendency of heterogeneous precipitation of η phase on the E particles is very strong since almost every E particle is covered by η phase. In Fig. 1(b) it is observed that coarse η particles are also formed at the grain boundaries that are enclosed by precipitate free zones (PFZ) with widths of about 15-20 nm. Fig. 2 shows the EDX-STEM elemental maps of the region highlighted by the white dashed box in Fig. 1(a). The composition of the E phase is measured as Al74.2-Zn3.1-Mg11.6-Cu1.8-Cr9.2 (at.%), the elemental content ratio of Al, Mg and Cr presents a specific value approximately 18:3:2, which is in good agreement with the stoichiometry of $Al_{18}Mg_3Cr_2$ (E phase). This composition also indicates that some Zn and Cu atoms are incorporated in the E phase. The heterogeneous precipitation of the η phase can also be evidenced by the enrichment of Mg, Zn and Cu atoms at the interface of the E particles. Detailed atomic resolution HAADF-STEM characterization is presented in the next section in order to reveal the atomic structure of the two phases.

Three typical examples of E particles are presented in Fig. 3. It can be seen that island-like or droplet-like η particles are distributed at the long edge of the lath E phase, while no or very few η particles are present at the short edge of the E phase. The structural identification of the η phase will be demonstrated in the next section. By statistic more than 20 E particles, it can be concluded that the long edge of the lath E particle is the preferential nucleation site of the η phase. The contact angles (θ) of the η phase formed at the E/Al interface vary from 30° to 70° measured as the projected angles. For all the three E particles in Fig.3, precipitate free zones (PFZ) with widths ranging from 20 nm to 40 nm are observed at the vicinity of the E phase. The presence of PFZ is detrimental to the mechanical properties of the 7075 alloy. Besides, some facets are observed for the E particle shown in Fig. 3(c). These facets are always associated with the nucleation of coarse η phase [18].

In order to reveal the heterogeneous precipitation mechanism of the η phase on the E particles, atomic-resolution HAADF-STEM and EDX mapping were performed for two E particles viewed along the $<\bar{1}12>_{Al}$ and $<011>_{Al}$ zone axes, respectively (Fig. 4). The two E particles exhibit different sizes and morphologies. It can be seen that the E particle shown in Fig. 4(a) has a rectangle morphology with a dimension of 50×30 nm^2, while the E particle shown in Fig. 4(d) has a lath morphology with dimension of 60×300 nm^2. The different sizes and morphologies of the E particles observed from different directions are probably related to the various morphologies of the E phase or different orientational views of the same particle. Atomic resolution HAADF-STEM images and corresponding FFT patterns of the two E particles are shown in Fig. 4(b, e) and (c, f), respectively, confirming the FCC nature of the particle. For the HAADF-STEM image shown in Fig. 4(b), the two lattice spacings are

measured as d_1 = 10.8 Å and d_2 = 15.2 Å, which are close to the lattice spacings $d_{(110)}$ = 10.3 Å and $d_{(100)}$ =14.5 Å of the E phase when viewed along the $<110>_E$ zone axis [14]. A twin can be observed within the E particle as indicated by the mirrored plane marked by the yellow dotted lines in Fig. 4(b) and the superposition of two <110> diffraction patterns in Fig. 4(c). This twin can be clearly identified as $(111)[11\bar{2}]$ as demonstrated by the FFT pattern shown in Fig. 4(c). For the HAADF-STEM image of the E particle shown in Fig. 3(e), the two lattice spacings are measured as d_3 = 4.31 Å and d_4 = 8.3 Å, which are close to the lattice spacing $d_{(220)}$ = 5.14 Å and $d_{(111)}$ = 8.39 Å of the E phase viewed along the $<112>_E$ zone axis. Therefore, the interplanar distances of the E particle correspond well with the previous literature [15]. The slight differences of interplanar distances are probably caused by the chemical composition change within the E particles.

The EDX mappings of the two E particles of Fig. 4 are presented in Fig. 5 and Fig. 6, respectively. The compositions of two E particles delimited by the white boxes are shown in Table 1. For the E particle presented in Fig. 5, except for the enrichment of Zn and Cu, an unexcepted enrichment of Ti is also found within the particle, while the content of Cr is reduced compared with the E particle presented in Fig. 2. This strongly indicates that the Ti atoms could partially replace the Cr atoms within the E phase. For the E particle shown in Fig. 6, it can be found that the amounts of Zn, Cu and Ti are very low within the E particle, indicating that fewer solute atoms are incorporated in the E particle. Besides, segregation of Ti atoms can be observed at the E/Al interface. The different compositions of the E particles indicate that the E phase is a high solubility phase, different substitutions of solute atoms could occur within the particle, depending on the local composition or strain environment. Similar variations of chemical composition within the E phase were also reported in previous works in literature [16]. The heterogeneous precipitation of the η phase can be clearly identified by the local enrichment of Mg, Zn and Cu at the interface between the E phase and Al matrix. For the composition of the η phase delimited by the white box shown in Table 1, the elemental content ratio of Zn, Mg and Cu presents a specific value of approximately 3:2:1. This indicates that the η phase has a composition of $(Zn_{1.5}Cu_{0.5})Mg$, in which the Cu atoms partially replace the Zn atoms within the η phase.

In order to reveal the OR between the E phase and the Al matrix, HAADF-STEM images are acquired at the E/Al interface with no or limited heterogeneous precipitation of η phase as presented in Fig. 7. According to the HAADF-STEM image and the corresponding FFT pattern of the E/Al interface shown in Fig. 7(a and b), only a very thin layer η phase is formed at the E/Al interface. The OR between the E phase and Al matrix is identified as: OR1: $[011]_E$ // $[\bar{1}12]_{Al}$, $(11\bar{1})_E$ // $(2\bar{4}3)_{Al}$. The lattice misfit along the $(11\bar{1})_E$ // $(2\bar{4}3)_{Al}$ plane is calculated as $\delta = | d(11\bar{1})_E - d(2\bar{4}3)_{Al} | / d(2\bar{4}3)_{Al} = |9.4269 - 7.502|/7.502 = 25.6\%$. In contrast, the HAADF-

STEM image and the corresponding FFT pattern of the E/Al interface shown in Fig. 7(c and d) indicate that no η phase is formed in this region. The OR between the E phase and Al matrix is identified as OR2: $[\bar{1}12]_E$ // $[011]_{Al}$, $(220)_E$ // $(34\bar{4})_{Al}$. The lattice misfit along the $(220)_E$ // $(34\bar{4})_{Al}$ plane is calculated as $\delta = |d(220)_E - d(34\bar{4})_{Al}|/d(34\bar{4})_{Al} = |6.369 - 5.137|/6.369 = 19.5\%$. This indicates that the E phase is incoherent with the Al matrix. Although the two E particles shown in Fig.7(a and c) were acquired along with different zone axes, it is clear that two different ORs are presented between the E particle and Al matrix.

3.2 Structure characteristic of the η phase

Enlarged HAADF-STEM images of the heterogeneously precipitated η phase marked by the white boxes in Fig. 4(a and d) are shown in Fig. 8. For the η phase in Fig. 8(a), it can be seen that it exhibits a R/R^{-1} stacking layer structure, which contains one rhombohedral-like unit (R) connecting with another rhombohedral-like unit (R^{-1}) rotated by 180° with respect to R, as indicated in the enlarged image of the region marked by the blue box in Fig. 8(a). Besides, in some regions of the η phase, stacking faults such as RR against the proper ordering of RR^{-1} can be seen. The existence of such stacking faults is not abnormal but rather common in the η precipitates. The observed η phase shows a same structure as the η_2 phase reported in the literature [6, 19]. The OR between the heterogeneously precipitated η phase and the Al matrix is identified as: $[\bar{1}12]_{Al}$ // $[2\bar{1}\bar{1}0]_\eta$, $(201)_{Al}$ // $(01\bar{1}0)_\eta$. The HAADF-STEM image and corresponding FFT pattern of the η_2 phase homogeneously precipitated in the Al matrix are shown in Fig. 8 (e and f). The OR between the η_2 phase and Al matrix can be identified as: $[\bar{1}12]_{Al}$ // $[2\bar{1}\bar{1}0]_\eta$, $(1\bar{1}1)_{Al}$ // $(01\bar{1}0)_\eta$. It is clear that the heterogeneously precipitated η phase exhibits a different OR compared with the η_2 phase formed in the Al matrix. The two ORs can be discriminated by a relative rotation of about 39° along $[2\bar{1}\bar{1}0]_\eta$. For the heterogeneously precipitated η phase presented in Fig. 8(c), it can be seen that the η phase exhibits the hexagonal stacking configuration of the $MgZn_2$ structure viewed along the $[0001]_\eta$ axis. This structure has the same structure as the $\eta_{4'}$ phase reported in previous literature [6]. Once again, due to the fact that the η phase and the Al matrix are not at the same focus, the lattice of the Al matrix is not visible in Fig. 8(c). By changing the focus of the image, we can still define the direction of the Al matrix, and the OR between the heterogeneously precipitated η phase and the Al matrix is identified as: $[011]_{Al}$ // $[0001]_\eta$, $(3\,4\bar{4})_{Al}$ // $(01\bar{1}0)_\eta$. The HAADF-STEM image and corresponding FFT pattern of the $\eta_{4'}$ phase homogeneously precipitated in the Al matrix are presented in Fig. 8(g and h). Its OR with the Al matrix can be identified as: $[011]_{Al}$ // $[0001]_\eta$, $(23\bar{3})_{Al}$ // $(01\bar{1}0)_\eta$, which is different from the OR shown in Fig. 8(c). The two ORs can be discriminated by a relative rotation of about 10° along the $[0001]_\eta$ axis. This implies that after

the heterogeneous precipitation on the E particles, the OR between the η phase and the Al matrix is changed.

3.3 Interface structure of the E/η/Al matrix

The HAADF-STEM images and the corresponding FFT patterns of the two E/η interfaces are presented in Fig. 9. For the E/η interface presented in Fig. 9(a), it can be seen that the η particles are heterogeneously precipitated along the $(111)_E$ plane of the E particle. The OR between the η and the E phase is identified as: $<2\bar{1}\bar{1}0>_\eta$ // $<011>_E$, $(0001)_\eta$ // $(1\bar{1}1)_E$, $(01\bar{1}0)_\eta$ // $(13\bar{3})_E$ from the FFT pattern showed in Fig. 9(b). The lattice misfit along the $(0001)_\eta$ // $(1\bar{1}1)_E$ plane is calculated as $\delta = | d(0001)_\eta - d(1\bar{1}1)_E | / d(1\bar{1}1)_E = |8.566-8.39|/8.39=2.1\%$, which indicates a good coherency of the E/η interface in this direction. From the IFFT image of the $(1\bar{1}1)_E$ planes shown in Fig. 9(c), it can be seen that a misfit dislocation is formed at the interface, this dislocation is caused by the irregular arrangement of the RR^{-1} stacking within the η phase as shown in Fig. 8(a). For the E/η interface presented in Fig. 9(d), the η particles are heterogeneously precipitated along the $(220)_E$ plane of the E particle. The OR between the η phase and the E phase is identified as: $[0001]_\eta$ // $[\bar{1}12]_E$, $(01\bar{1}0)_\eta$ // $(220)_E$ from the FFT pattern shown in Fig. 9(e). The lattice misfit along the $(1010)_\eta$ // $(220)_E$ plane is calculated as $\delta = |d(1010)_\eta - d(220)_E| = |(5.22-5.14)|/5.14 = 1.5\%$, indicating that a coherent interface is formed along the $(1010)_\eta$ // $(220)_E$ plane. The IFFT image of the $(1\bar{1}1)_E$ planes presented in Fig. 9(f) also shows the absence of lattice dislocations at the E/η interface along the $(0001)_\eta$ // $(112)_E$ plane. It is clear that after the heterogeneous precipitation of the η phase on the E particles, the incoherent E/Al interfaces are replaced by coherent E/η interfaces.

To further understand the heterogeneous precipitation mechanism of the η phase, enlarged HAADF-STEM images of the two E/η interfaces marked by the white boxes in Fig. 9(a and d) are shown in Fig. 10(a and d). For the E/η interface with the $(0001)_\eta$ // $(1\bar{1}1)_E$ plane shown in Fig. 10(a), it can be clearly seen that the interface exhibits a zig-zag structure. The formation of a large number of nano-sized facets in the E/η interface is mainly caused by the periodic arrangement of RR^{-1} stacking within the η phase. The substructure of the rhombohedral-like unit (R) is stable and does not break at the E/η interface. A schematic illustration of this interface shown in Fig. 10(c) clearly presents the relationship between the RR^{-1} stacking and the zig-zag structure of the interface. In the region that contains a stacking fault with the RR arrangement, the lengths and angles of the zig-zag structure of the E/η interface are changed. Some flattened-hexagons, flattened-pentagons and triangles are formed in the RR staking region of the E/η interface. From the contrast colouring HAADF-STEM image shown in Fig. 10(b), it can be seen that the Zn columns of the η phase close to the E/η interface have a lower contrast than the Zn columns inside the η phase as indicated by the dotted white lines. In

contrast, the Cr columns of the E phase close to the E/η interface have higher contrast than the Cr columns in the E phase as indicated by the dotted yellow lines. This indicates that mutual diffusion occurred between the two phases. Some Zn atoms diffuse into the E phase as indicated by the EDX results shown in Fig. 5(c), while some Cr atoms are supposed to be incorporated in the η phase. However, the EDX mapping shown in Fig. 5(f) does not show the presence of Cr atoms within the η phase, which can be explained by the small size of the η phase. Regarding the E/η interface along the $(01\bar{1}0)_{\eta}$ // $(220)_{E}$ plane shown in Fig. 10(d), it can be seen that the E/η interface is very straight and of high coherency. The schematic illustration of this interface presented in Fig. 10(f) also confirms the good coherency between the two phases. From the adjusted HAADF-STEM shown in Fig. 10(e), it can be observed that the Zn columns of the η phase close to the interface have a lower contrast than the Zn columns inside the η phase. Although contrast changes within the E phase cannot be clearly resolved in this region, it can still be deduced that mutual diffusion occurred at this interface as evidenced by the presence of Zn atoms within the E particles, as shown in the EDX map of Fig. 6(c). The mutual diffusion of solute atoms can further increase the coherency of the E/η interface by reducing the chemical interface energy[20].

4. Discussion

It is clear that the tendency of heterogeneous precipitation of the η phase on the E dispersoid is very strong so that almost every E particle is covered by island-like or droplet-like η phase. The underlying mechanisms of the heterogeneous precipitation at the E/η interfaces are discussed in detail below. Based on the classical nucleation theory for the homogeneous precipitation, the minimum activation energy barrier ΔG^*_{hom} can be obtained by the equation [18]:

$$\Delta G^*_{hom} = -\frac{16\pi\gamma^3_{\alpha\beta}}{3(\Delta G_V - \Delta G_S)^2}$$

where $\gamma_{\alpha\beta}$ and ΔG_S are the interfacial energy and strain energy of the precipitate, respectively. ΔG_V is the difference in free energy of the precipitate and the Al matrix. For the heterogeneous precipitation at the E/Al interface, the minimum activation energy barrier ΔG^*_{het} is calculated by:

$$\Delta G^*_{het} = -\frac{4}{3}\pi\frac{\gamma^3_{\alpha\beta}}{(\Delta G_V - G_S)^2}(2 - 3\cos\theta + \cos^3\theta)$$

where θ is the contact angle between the η phase and the E particle. The relationship between ΔG^*_{hom} and ΔG^*_{het} is obtained using the following equation:

$$\frac{\Delta G_{het}^{*}}{\Delta G_{hom}^{*}} = \frac{1}{4}(2 - 3\cos\theta + \cos^3\theta) = f(\theta)$$

Thus, as long as the contact angle between the η phase and the E phase is smaller than 180°, the calculated $f(\theta)$ is smaller than 1, which means that the energy barrier for the heterogeneous precipitation at the E/Al interface is decreased compared with the homogeneous precipitation in the Al matrix.

The heterogeneous precipitation of the η phase on the E particle is mainly due to the incoherent interface between the E phase and the Al matrix. The incoherent E/Al interface has a rather high interface energy and thus is energetically unstable. The nucleation of the η phase on the E particle can stabilize the E/Al interface by introducing a coherent E/η interface, which can significantly reduce the overall energy. Therefore, the drive force for the heterogeneous precipitation of η phase on the E particle is very high. As presented in Fig. 7, the E particle exhibits two different ORs with the Al matrix, which result in two different ORs between the η phase, E phase and Al matrix. Two different ORs between the η, E and Al matrix are identified: OR1 $[2\bar{1}\bar{1}0]_{\eta}$// $[011]_{E}$ // $[\bar{1}12]_{Al}$, $(01\bar{1}0)_{\eta}$ // $(13\bar{3})_{E}$ // $(201)_{Al}$, OR2 $[\bar{1}12]_{E}$ // $[0001]_{\eta}$// $[011]_{Al}$, $(01\bar{1}0)_{\eta}$ // $(220)_{E}$ // $(34\bar{4})_{Al}$. For both the OR1 and OR2, the OR of the heterogeneously precipitated η phase with the Al matrix is changed compared with the homogeneously precipitated η phase in the Al matrix. The two new ORs of the η phase with the Al matrix are inconsistent with the 11 ORs reported in the literature [6]. The OR1 corresponds to a rotation of 39° along the $[2\bar{1}\bar{1}0]_{\eta}$ direction with respect to the η_2 phase, while the OR2 corresponds to a rotation of about 10° along the along $[0001]_{\eta}$ direction with respect to the $\eta_{4'}$ phase. The reorientation of the heterogeneously precipitated η phase occurs in order to obtain a good coherency between the η phase and E particle. Besides, the mutual diffusion observed in the region close to the E/η interface can further reduce the chemical interface energy of the E/η interface. Therefore, the heterogeneous precipitation of η phase is favoured at the interface of the E phase.

The heterogeneous precipitation of the η phase on the E particle can significantly increase the quench sensitivity of the 7075 alloy. The formation of coarse η phase on the E phase consumes the solute atoms and vacancies in the matrix, which reduces the age-hardening response. Besides, the depletion of solute atoms and vacancies in the region close to the E particle will lead to the formation of a PFZ surrounding the E particle. The presence of a PFZ can cause strain localization at the E/η/Al interface, which results in low ductility and fracture toughness of the alloy [21, 22]. Therefore, the heterogeneous precipitation of the η phase on the E particle is detrimental to the strength and fracture resistance of the alloy. Substantial efforts have been devoted to decrease the quench sensitivity of the Al-Zn-Mg-Cu alloy by

suppressing the heterogeneous precipitation of the η phase, however, few achievements have been made so far [7, 8, 23]. Based on the present finding that the incoherent E/Al interface is responsible for the high tendency of heterogeneous precipitation of the η phase, increasing the coherency of the E/Al interface can be considered as a promising method to mitigate or suppress the heterogeneous precipitation. Adding some specific micro-alloying elements which can decorate the E/Al interface and increase its coherency is possibly a feasible method to suppress the negative effect of heterogeneous precipitation.

5. Conclusions

In this work, the heterogeneous precipitation of the η phase on the E particle is systematically investigated in a 7075 aluminum alloy by atomic scale HAADF-STEM characterization. The following conclusions can be drawn:

1. Island-like or droplet-like η particles are hetergeneously precipitated on the E dispersoid, which consume solute atoms, form a PFZ in the region close to the E particle and thus are detrimental to the strength, ductility and fracture toughness of the 7075 alloy.
2. Two different ORs between the η, E and Al matrix are identified: OR1 $[2\bar{1}\bar{1}0]_\eta$ // $[011]_E$ // $[\bar{1}12]_{Al}$, $(01\bar{1}0)_\eta$ // $(13\bar{3})_E$ // $(201)_{Al}$, OR2 $[\bar{1}12]_E$ // $[0001]_\eta$// $[011]_{Al}$, $(01\bar{1}0)_\eta$ // $(220)_E$ // $(3\,4\bar{4})_{Al}$. The η phase is preferentially nucleated along the $\{111\}_E$ or $\{220\}_E$ planes, depending on its OR. The incoherent E/Al interface is responsible for the high tendency of heterogeneous precipitation. The heterogeneous nucleation of the η phase on the E particle can stabilize the E/Al interface by introducing the coherent E/η interface.
3. The ORs between the heterogeneously precipitated η phase and the Al matrix are rotated with respect to the OR between the homogeneously precipitated η phase and the Al matrix. Mutual diffusion of the Zn, Cu and Cr atoms occurs in the region close to the E/η interface. The reorientation of η phase and mutual diffusion of solute atoms can improve the coherency of the E/η interface.
4. Increasing the coherency of the E/Al interface is a promising method to suppress the heterogeneous precipitation of the η phase.

Acknowledgments

This work was supported by the Natural Science Foundation of Jiangsu Province (SBK2020042102) and the Fundamental Research Funds for the Central Universities of China (Project No. 2020CDJDPT001).

Reference

[1] M.J. Starink, S.C. Wang, Acta Mater. 51 (2003) 5131-5150.

[2] T. Marlaud, A. Deschamps, F. Bley, W. Lefebvre, B. Baroux, Acta Mater. 58 (2010) 248-260.
[3] M. Liu, B. Klobes, K. Maier, Scr. Mater. 64 (2011) 21-24.
[4] J.Z. Liu, J.H. Chen, X.B. Yang, S. Ren, C.L. Wu, H.Y. Xu, J. Zou, Scr. Mater. 63 (2010) 1061-1064.
[5] X.Z. Li, V. Hansen, J. GjØnnes, L.R. Wallenberg, Acta Mater. 47 (1999) 2651-2659.
[6] T.F. Chung, Y.L. Yang, M. Shiojiri, C.N. Hsiao, W.C. Li, C.S. Tsao, Z. Shi, J. Lin, J.-R. Yang, Acta Mater. 174 (2019) 351-368.
[7] M. Fourmeau, C.D. Marioara, T. Børvik, A. Benallal, O.S. Hopperstad, Philos. Mag. 95 (2015) 3278-3304.
[8] B. Cai, B.L. Adams, T.W. Nelson, Acta Mater. 55 (2007) 1543-1553.
[9] Z. Li, H. Jiang, Y. Wang, D. Zhang, D. Yan, L. Rong, J Mater. Sci.Technol. 34 (2018) 1172-1179.
[10] A.M. Cassell, J.D. Robson, C.P. Race, A. Eggeman, T. Hashimoto, M. Besel, Acta Mater. 169 (2019) 135-146.
[11] H.C. Fang, K.H. Chen, X. Chen, L.P. Huang, G.S. Peng, B.Y. Huang, Mater. Sci. Eng. A. 528 (2011) 7606-7615.
[12] M. Li, Y. Yang, M. Han, W. Zhang, B. Huang, X. Luo, J. Ru, Acta Metall. Sin-Engl. 27 (2014) 677-681.
[13] S.T. Lim, S.J. Yun, S.W. Nam, Mater. Sci. Eng. A. 371 (2004) 82-90.
[14] M. Kanno, I. Araki, Q. Cui, Mater Sci Tech 10 (1994) 599-603.
[15] S. Samson, Nature 173 (1964) 1185-1186.
[16] R. Ayer, J.Y.Koo, J.W.Steeds, B.K.Park, Metall. Trans. A 16 (1985) 1925-1936.
[17] M. Svoboda, J. Janovec, M. Jenko, A. Vrankovi, Mtaec 38 (2004) 289-294.
[18] Y. Ma, A. Addad, G. Ji, M.-X. Zhang, W. Lefebvre, Z. Chen, V. Ji, Acta Mater. 185 (2019) 278-299.
[19] C.D. Marioara, W. Lefebvre, S.J. Andersen, J. Friis, J Mater. Sci. 48 (2013) 3638-3651.
[20] A.J. Ardell, Acta Mater. 61 (2013) 7828-7840.
[21] T.F. Morgeneyer, M.J. Starink, S.C. Wang, I. Sinclair, Acta Mater. 56 (2008) 2872-2884.
[22] B. Milkereit, M.J. Starink, P.A. Rometsch, C. Schick, O. Kessler, Materials (Basel) 13 (2020) 2554-2565.
[23] S. Liu, C. Li, S. Han, Y. Deng, X. Zhang, J Alloy Compd. 625 (2015) 34-43.

Figure captions

Fig. 1 Low-magnification HAADF-STEM images of typical regions in the over-aged 7075 alloy.

Fig. 2 EDX-STEM elemental maps of the region highlighted by the white dashed box of Fig. 1(a). The Al map in (a) do not show high signal of Al within the E particle probably relate to its relative intensity when compared to the matrix.

Fig.3 Low-magnification HAADF-STEM images of three typical examples of η phase formed at the E/Al interface.

Fig.4 (a, d) Low-magnification HAADF-STEM, atomic resolution HAADF-STEM images and corresponding FFT patterns of two E particles viewed along the $<011>_{Al}$ and $<\bar{1}12>_{Al}$ zone axes, respectively. (b and e) are taken at the regions marked by the blue boxes shown in (a and d). The FFT patterns of (b, f) are obtained from HAADF-STEM images presented in (b, e).

Fig. 5 EDX mappings of the E particle presented in Fig. 4(a)

Fig. 6 EDX mappings of the E particle presented in Fig. 4(d)

Fig. 7 (a, c) HAADF-STEM image and (b, d) corresponding FFT pattern of the E/Al interface

Fig. 8 Atomic resolution HAADF-STEM images and corresponding FFT patterns of the heterogeneously precipitated (a-d) η phase and (e-f) η_2 and (g-h) η_4 phase homogeneously precipitated in the Al matrix.

Fig. 9 (a, d) HAADF-STEM images and (b, e) corresponding FFT patterns of the two E/η interfaces. (c and f) show the IFFT image of the $(1\bar{1}1)_E$ planes of the two interfaces.

Fig. 10 (a, d) Enlarged HAADF-STEM images of the two E/η interfaces marked by the white boxes in Fig. 9(a and d), (b and e) are the contrast coloured HAADF-STEM images of (a, d), (c and f) are the schematic illustrations of the two interfaces.

Table Caption

Table 1 STEM-EDX composition (at.%) measurement of the two E particles and η phase shown in Figs. 5 and 6. The measurements were obtained in the zones indicated by white squares in Fig. 5(a) and Fig. 6(a).

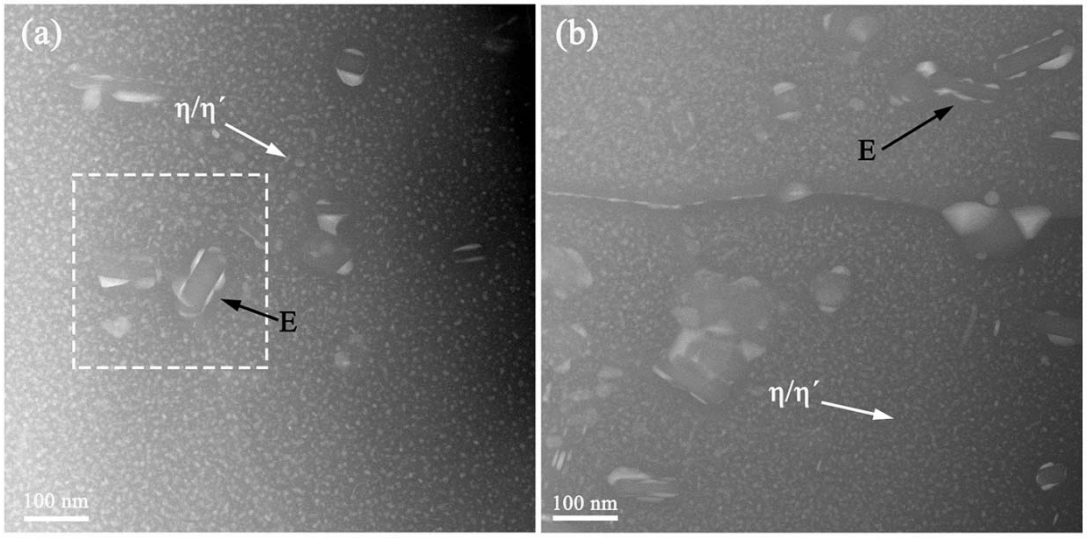

Fig. 1 Low-magnification HAADF-STEM images of typical regions in the over-aged 7075 alloy.

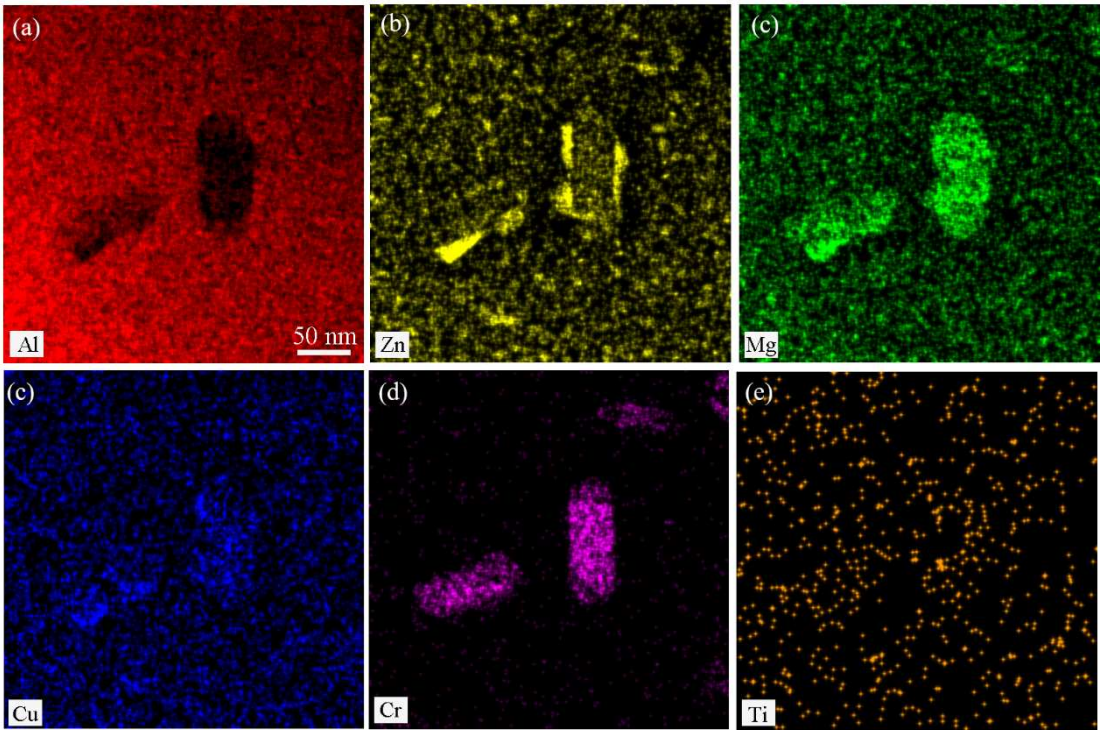

Fig. 2 EDX-STEM elemental maps of the region highlighted by the white dashed box of Fig. 1(a). The Al map in (a) do not show high signal of Al within the E particle probably relate to its relative intensity when compared to the matrix.

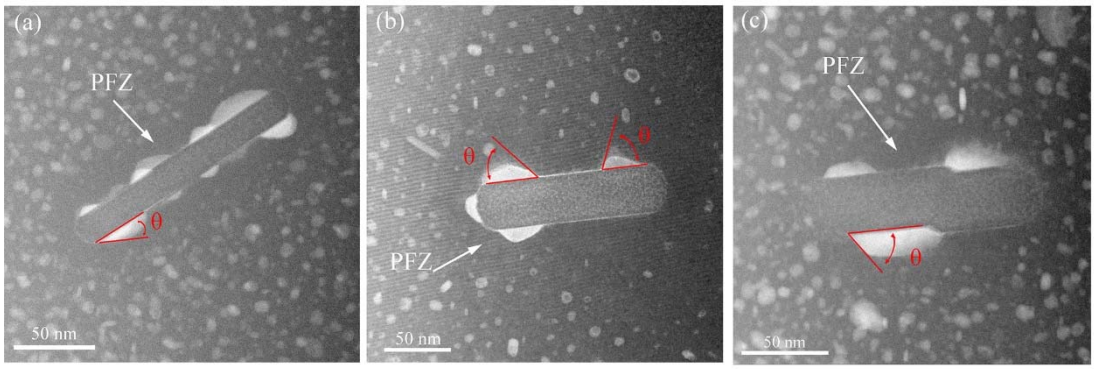

Fig.3 Low-magnification HAADF-STEM images of three typical examples of η phase formed at the E/Al interface.

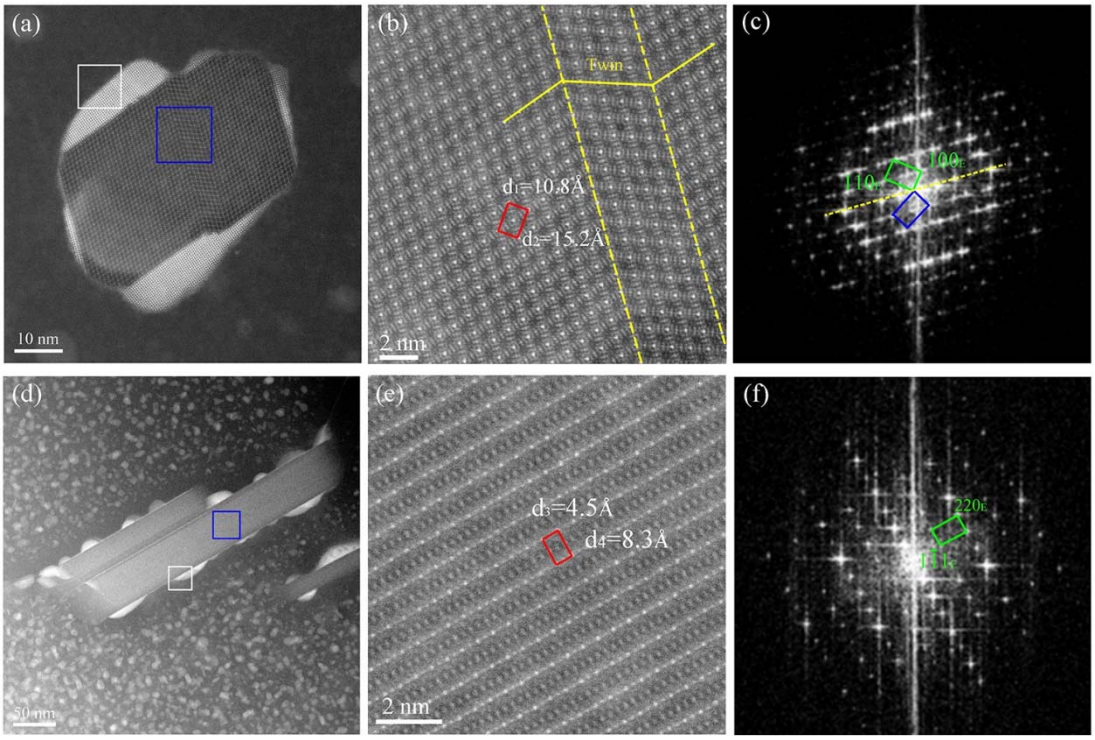

Fig.4 (a, d) Low-magnification HAADF-STEM, atomic resolution HAADF-STEM images and corresponding FFT patterns of two E particles viewed along the $<011>_{Al}$ and $<\bar{1}12>_{Al}$ zone axes, respectively. (b and e) are taken at the regions marked by the blue boxes shown in (a and d). The FFT patterns of (b, f) are obtained from HAADF-STEM images presented in (b, e).

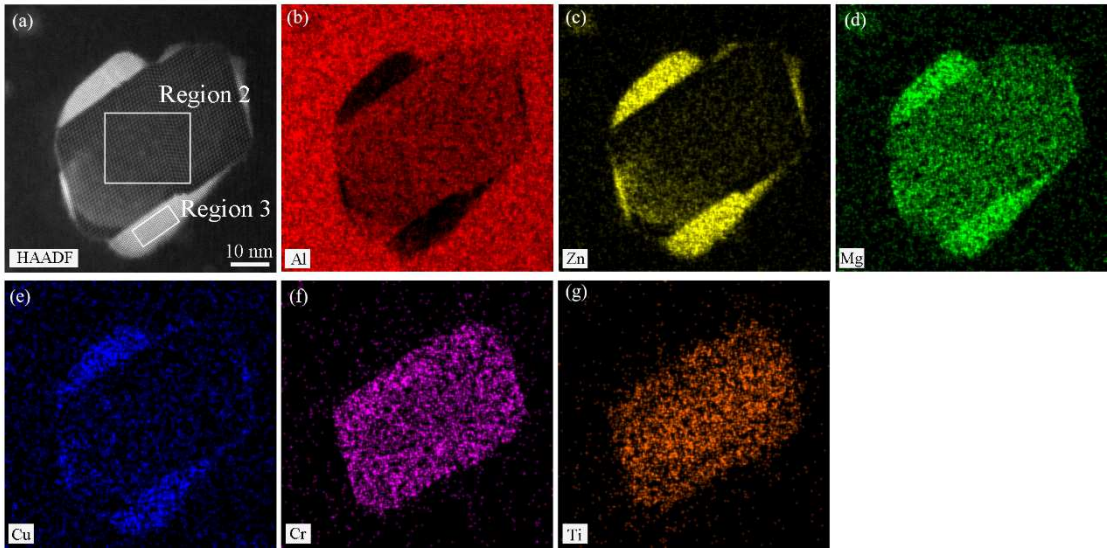

Fig. 5 EDX mappings of the E particle presented in Fig. 4(a)

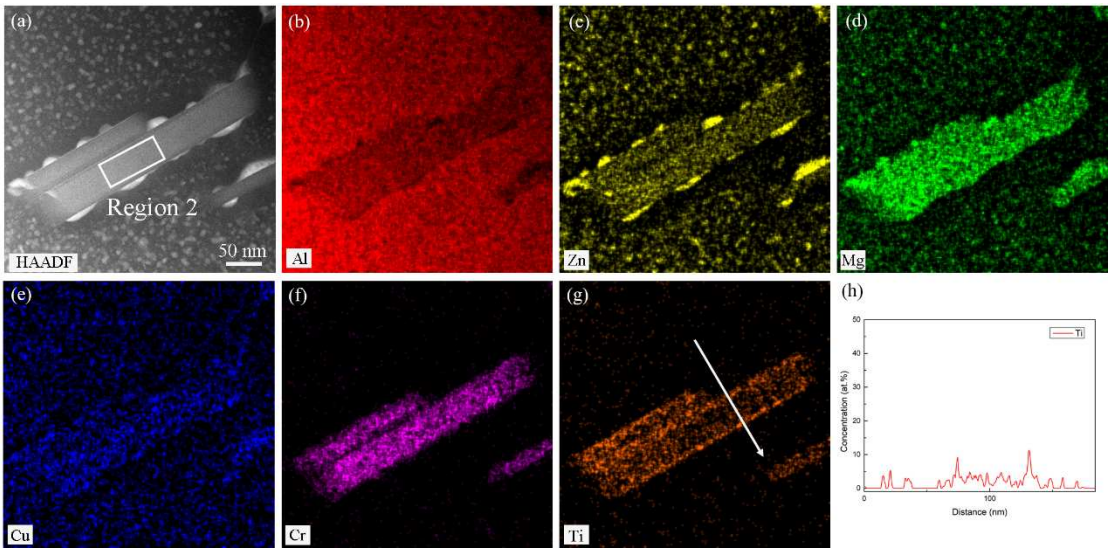

Fig. 6 EDX mappings of the E particle presented in Fig. 4(d)

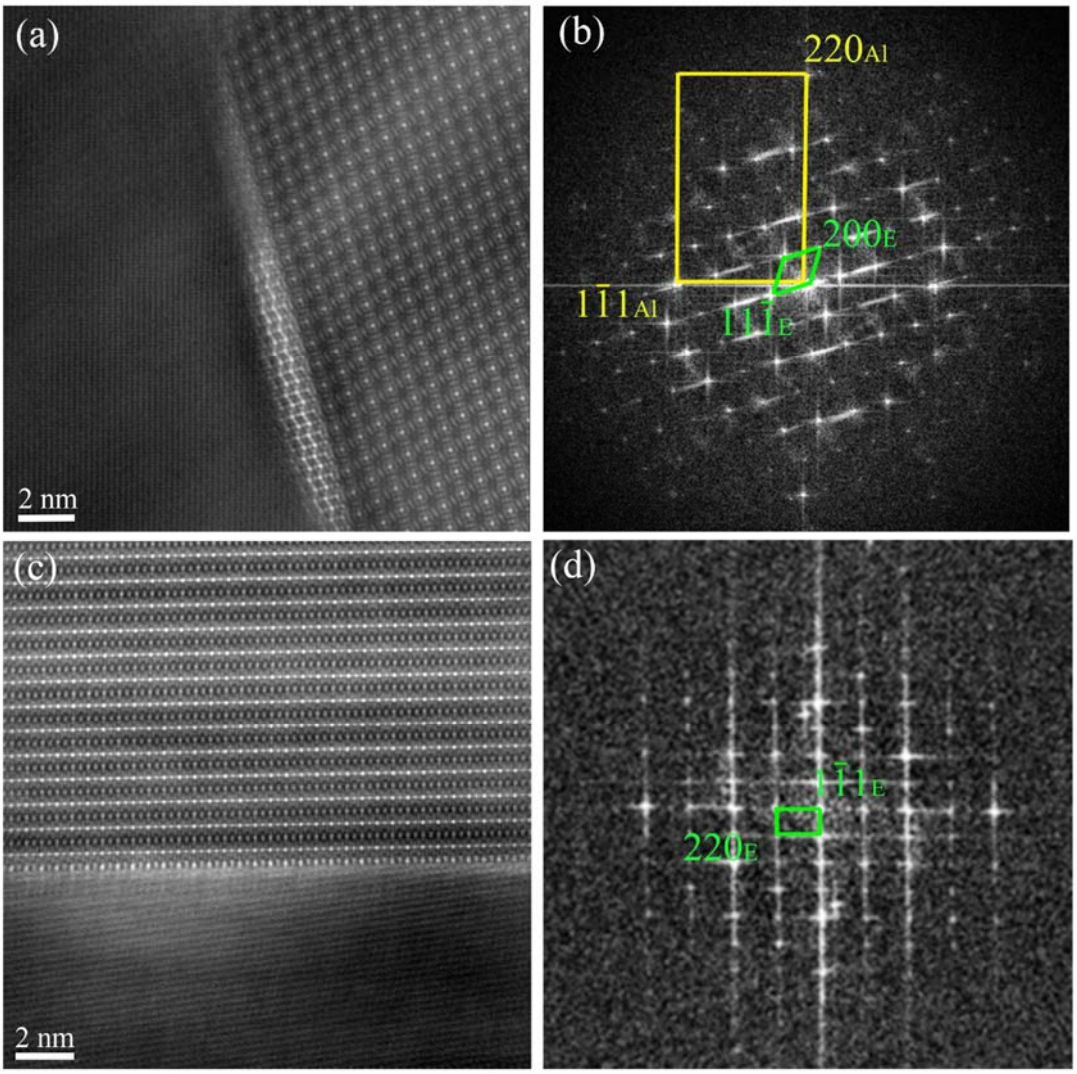

Fig. 7 (a, c) HAADF-STEM image and (b, d) corresponding FFT pattern of the E/Al interface

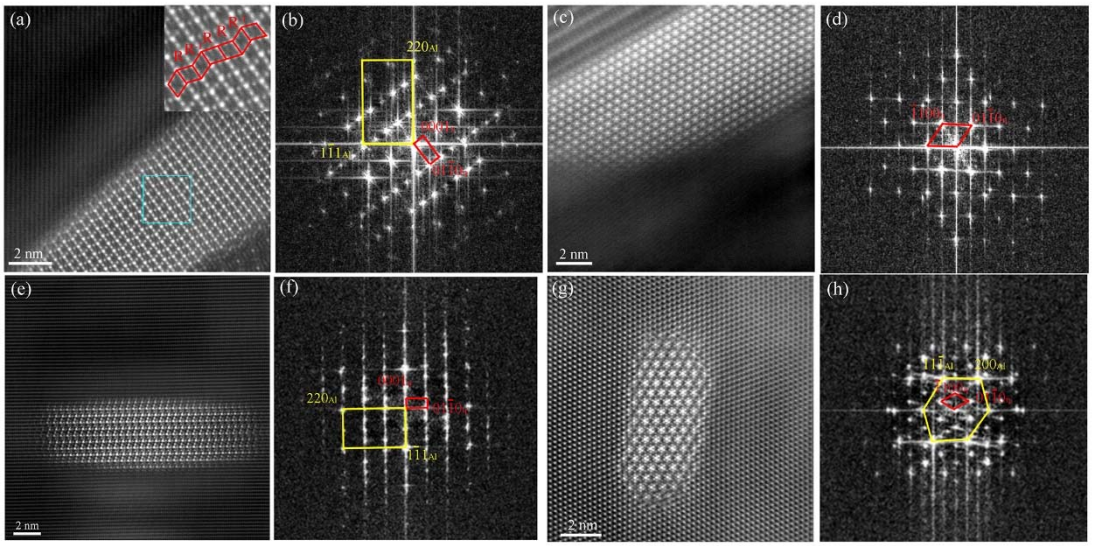

Fig. 8 Atomic resolution HAADF-STEM images and corresponding FFT patterns of the heterogeneously precipitated (a-d) η phase and (e-f) η_2 and (g-h) η_4 phase homogeneously precipitated in the Al matrix.

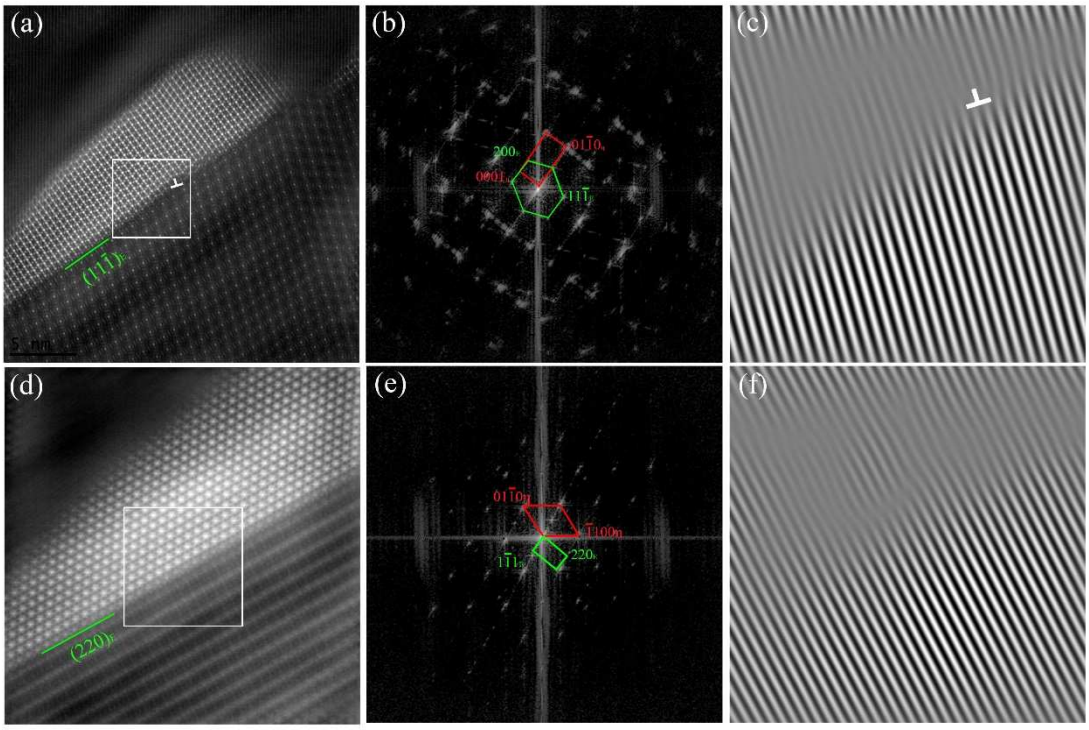

Fig. 9 (a, d) HAADF-STEM images and (b, e) corresponding FFT patterns of the two E/η interfaces. (c and f) show the IFFT image of the $(1\bar{1}1)_E$ planes of the two interfaces.

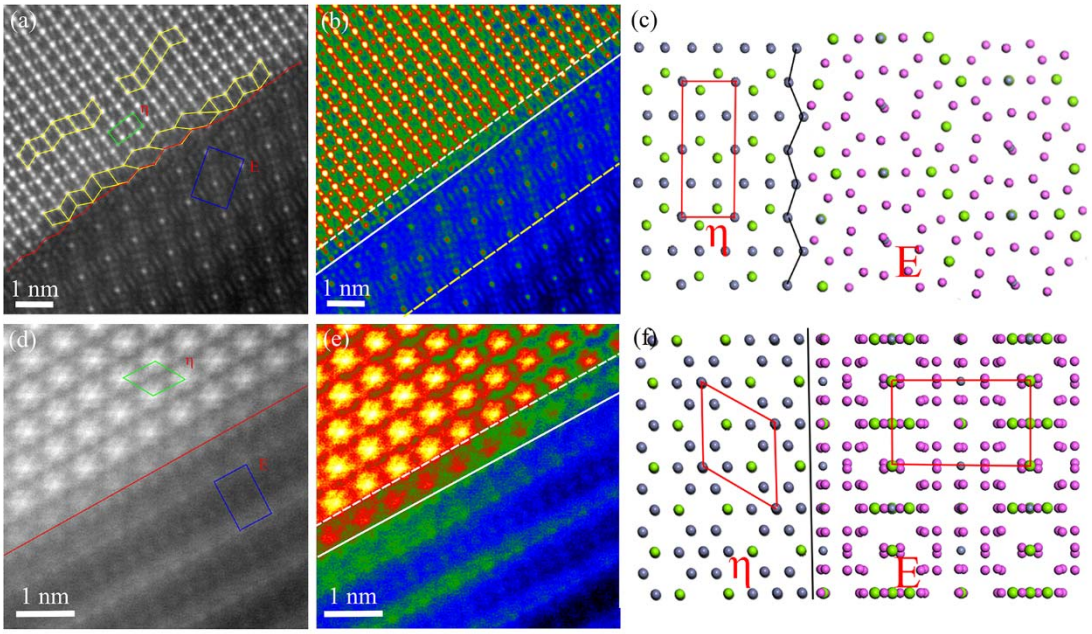

Fig. 10 (a, d) Enlarged HAADF-STEM images of the two E/η interfaces marked by the white boxes in Fig. 9(a and d), (b and e) are the contrast coloured HAADF-STEM images of (a, d), (c and f) are the schematic illustrations of the two interfaces.

Table 1 STEM-EDX composition (at.%) measurement of the two E particles and η phase shown in Figs. 5 and 6. The measurements were obtained in the zones indicated by white squares in Fig. 5(a) and Fig. 6(a).

	Al	Zn	Mg	Cu	Cr	Ti
Region 1	66.5	5.3	15.4	2.0	6.1	4.6
Region 2	80.6	0.7	14.1	0.2	4.3	0.1
Region 3	63.1	15.8	11.6	6.3		